

Hydrogel-Based, Dynamically Tunable Plasmonic Metasurfaces

Jian Zhang

Institute of Advanced Magnetic Materials, College of Materials and Environmental Engineering, Hangzhou Dianzi University, Hangzhou, 310018, China

Qiang Li

Zhejiang University <https://orcid.org/0000-0001-9344-6682>

Chenjie Dai

Electronic Information School, Wuhan University, Wuhan 430072, China

Mingliang Cheng

Hangzhou Dianzi University

Xin Hu

Suzhou Institute of Nano-Tech and Nano-Bionics (SINANO), Chinese Academy of Sciences

Hyun-Sik Kim

Hongik University

Heesun Yang

Hongik University

Daniel Preston

Rice University <https://orcid.org/0000-0002-0096-0285>

Zhongyang Li

Wuhan University

Xuefeng Zhang

Hangzhou Dianzi University

Won-Kyu Lee (✉ wklee@hongik.ac.kr)

Hongik University <https://orcid.org/0000-0002-7878-1981>

Article

Keywords:

Posted Date: April 12th, 2022

DOI: <https://doi.org/10.21203/rs.3.rs-1548679/v1>

License: © ⓘ This work is licensed under a Creative Commons Attribution 4.0 International License.

[Read Full License](#)

Hydrogel-Based, Dynamically Tunable Plasmonic Metasurfaces

Jian Zhang,^{1,†} Qiang Li,^{2,†} Chenjie Dai,^{3,†} Mingliang Cheng,¹ Xin Hu,¹ Hyun-Sik Kim,⁴
Heesun Yang,⁴ Daniel J. Preston,⁵ Zhongyang Li,^{3,*} Xuefeng Zhang,^{1,*} Won-Kyu Lee^{4,*}

¹ Information Research Center for EM Metamaterials and Institute of Advanced Magnetic Materials, College of Materials and Environmental Engineering, Hangzhou Dianzi University, Hangzhou 310018, PR China

² State Key Laboratory of Modern Optical Instrumentation, College of Optical Science and Engineering, Zhejiang University, Hangzhou 310027, PR China

³ Electronic Information School, Wuhan University, Wuhan, 430072, PR China

⁴ Department of Materials Science and Engineering, Hongik University, Seoul 04066, Korea

⁵ Department of Mechanical Engineering, Rice University, Houston, Texas 77006, USA

[†]Authors who contributed equally to this work

*Corresponding author: zhongyangli@whu.edu.cn; zhang@hdu.edu.cn; wklee@hongik.ac.kr

Abstract

Flat metasurfaces with subwavelength meta-atoms can be designed to manipulate the electromagnetic parameters of incident light and enable unusual light-matter interactions beyond the capabilities of the constituent materials themselves. Although hydrogel-based metasurfaces have the potential to control optical properties dynamically in response to environmental conditions, the pattern resolution of these surfaces has typically been limited to microscale features or larger, limiting capabilities at the nanoscale and precluding effective use in metamaterials. This paper reports a general approach to developing reversibly tunable plasmonic metasurfaces with hydrogel meta-atoms at the subwavelength scale. Periodic arrays of hydrogel nanodots with continuously tunable diameters between 180 nm and 240 nm were fabricated on silver substrates, resulting in humidity-responsive surface plasmon polaritons (SPPs) at the nanostructure-metal interfaces. The peaks of the SPPs were controlled reversibly by absorbing or releasing water within the hydrogel matrix; the matrix subsequently generated plasmonic color rendering in the visible spectrum. We demonstrated that metasurfaces designed with these spatially patterned nanodots of varying sizes can benefit applications in anti-counterfeiting and generate multicolored displays with single-nanodot resolution. Furthermore, we showed system versatility exhibited by broadband beam-steering on a phase modulator consisting of hydrogel supercell units in which the size variations of constituent hydrogel nanostructures engineer the wavefront of reflected light from the metasurface.

36 Flat metasurfaces with subwavelength meta-atoms (i.e., nanoscale unit cells analogous to
37 atoms) can manipulate electromagnetic parameters including amplitude, frequency, phase, and
38 polarization of incident light¹⁻³. The optical responses of these metasurfaces are tailored by
39 engineering the shape and size of the meta-atoms as well as their arrangements on the substrates,
40 enabling responses that are not possible with conventional optics^{4,5}. Designing plasmonic
41 metasurfaces with (semi-)metallic meta-atoms can go a step further than approaches relying on
42 dielectric metasurfaces by optimizing local-field enhancement of the surfaces in the sub-
43 diffraction limit⁶⁻⁸. In particular, the ability to control the geometric configurations of
44 plasmonic meta-atoms reversibly is critical for applications that require real-time light
45 manipulation, such as dynamic displays, chemical and biological sensing, optical cloaking, and
46 encryption⁹⁻¹². Both the intensity and quality factor of the plasmonic coupling over target
47 wavelength spectrums can be tuned by changing the surface material components (e.g.,
48 reconfigurable meta-atoms on deformable substrates) and the surrounding media¹³⁻¹⁶.

49 Use of active media surrounding the material components stands out as a particularly
50 promising approach to achieving dynamically tunable plasmonic metasurfaces¹⁶⁻¹⁸. Controlling
51 the refractive index of the media by external stimuli, such as solvent exchange and application
52 of electric fields, enables plasmonic resonance over a range of wavelengths that can be altered
53 or adjusted in a reversible manner^{18,19}. For example, birefringent liquid crystals (LCs) on
54 plasmonic surfaces can change their molecular orientation upon application of electric fields;
55 the consequent change of the effective refractive index leads to tunable resonance²⁰. Although
56 reversible and dynamic control over plasmonic coupling has been shown, the metamaterials
57 used in prior demonstrations require complicated fabrication and packaging processes to

58 integrate their constituent material components with the active media²¹⁻²³.

59 Controlling the states of phase-change materials, such as chalcogenides and vanadium
60 oxide, combined with plasmonic nanostructures, represents an alternative approach for media-
61 free, dynamic metasurfaces²⁴⁻²⁶. For example, the refractive index of VO₂ is switchable by
62 applying heat or electric current, and can in turn adjust the intensity and phase of plasmonic
63 resonance^{26,27}. The precise pattern placement of phase-changing meta-atoms, however, is often
64 challenging, especially at the nanoscale due to the limitations of etching processes on inorganic
65 material systems^{28,29}. Nanoscale patterning of the material components is critical to realize
66 dynamic metasurfaces that can modulate the plasmonic resonance continuously from
67 microwave to visible ranges^{30,31}. Recently, active nanoplasmonic devices based on metal
68 hybrids (e.g. MgH₂ and TiH₂) switched their optical properties in response to hydrogen
69 exposure and achieved full-color rendering, but additional infrastructure to control and measure
70 the safe flow of hydrogen is inevitable^{32,33}.

71 Hydrogels with hydrophilic molecular chains interconnected in three dimensions are
72 capable of retaining large amounts of water within their internal networks^{34,35}. By absorbing or
73 releasing water through the application of external stimuli (e.g., humidity, temperature, pH),
74 hydrogels can change the volume of their matrix by swelling or shrinking with a level of
75 deformability not attainable by other aqueous media³⁶⁻³⁸. Compared with the phase-change
76 materials, which switch their optical properties between two distinct phases, hydrogels deform
77 continuously and thereby generate gradients of optical properties³⁹⁻⁴¹. Tuning the plasmonic
78 responses among meta-atoms embedded by hydrogels has been demonstrated by changing the
79 spacing between meta-atoms and the effective reflective index through the deformation of the

80 hydrogel matrix. For example, continuous swelling of hydrogels can provide dynamic
81 structural coloration by the geometric changes of embedded photonic crystals and the shifting
82 of their photonic band gaps⁴²⁻⁴⁴. A general platform for dynamic metasurfaces can therefore
83 build upon technological advances through which designing the geometric configurations of
84 hydrogel meta-atoms is arbitrarily possible. Patterning size, shape, and the arrangement of
85 hydrogels, however, has remained limited to microscale areas or larger using conventional 3D
86 printing and optical processes based on UV-vis light sources⁴⁵⁻⁴⁷.

87 In this work, we show hydrogel-based, dynamically tunable plasmonic metasurfaces by
88 patterning hydrogel meta-atoms at the subwavelength scale using electron-beam lithography.
89 Polyvinyl alcohol was used as a high-resolution hydrogel resist to enable electron-beam
90 irradiation on the hydrogel molecules within nanoscale spots, resulting in hydrogel
91 nanostructures with precisely tunable size formed on silver (Ag) thin films. By absorbing or
92 releasing water within the hydrogel matrix (and thus giving rise to swelling or shrinking of the
93 nanostructures, respectively), both the volume of the meta-atoms and their spacing could be
94 reversibly tuned as a function of environmental humidity. The periodic arrays of hydrogel
95 nanostructures on the Ag films induced surface plasmonic polaritons and generated plasmonic
96 color rendering in the visible range between 505 nm to 600 nm. We demonstrated that the meta-
97 atoms respond to different levels of moisture in a stepwise manner, providing dynamic color
98 generation for anti-counterfeiting applications. Furthermore, we confirmed system versatility
99 by performing beam-steering on metasurfaces consisting of hydrogel supercell units in which
100 the changes in size of constituent hydrogel nanodots modulate the plasmonic phase shift and
101 the wavefront of the incident light.

102 **Results**

103 **Fig. 1a** depicts the fabrication processes to form hydrogel-based plasmonic metasurfaces,
104 in which hydrogel nanodots are periodically arranged on Ag sublayers. We achieved uniform
105 patterning of the hydrogel meta-atom arrays at the nanoscale with well-defined feature
106 characteristics, i.e., diameter (D), height (H), and periodicity (P), using electron-beam
107 lithography (EBL) with polyvinyl alcohol (PVA) layers of 150 nm thickness as hydrogel resists
108 (Fig. 1b). Conventional techniques to pattern hydrogels have relied on UV exposure,
109 nanoimprinting, and 3D printing, and the resulting pattern resolution has been limited to
110 hundreds of nanometers at the smallest^{45,47-49}. In this work, we irradiated the electron beam on
111 the hydrogel molecules within nanoscale spots, through which the materials could be patterned
112 into arbitrary shapes with a resolution of ~ 50 nm⁵⁰. By increasing the electron-beam exposure
113 dose on PVA layers from 1.26 to 6.35 pC/dot (at an exposure voltage of 2 kV), we continuously
114 tuned D from 180 nm to 240 nm (**Fig. 1c** and **Fig. S1**). This tunability was possible because
115 we controlled the distribution of the exposure energy as a radial function of the distance from
116 the beam point based on the forward-scattering of electrons⁵¹. Linear control over D was
117 achieved with the same H (of 150 nm) and P (of 400 nm), indicating that we could manipulate
118 the structural parameters independently and thereby design unlimited configurations of
119 combinatorial hydrogel nanostructures.

120 The periodic nanodot arrays on Ag generated surface plasmon polaritons (SPPs) which
121 are excited at the dielectric-metal interfaces formed by the grating momentum of the nanodot
122 lattice, with this mechanism being the basis for tunable structural coloration (**Figs. 1d-e**). Here
123 we selected Ag to support SPPs because highly reflective Ag films typically induce strong

124 resonance over the entire visible spectrum⁵². We showed that the resonant peak red-shifted
 125 from 498 nm to 585 nm as D increased from 188 to 237 nm (**Fig. 1d**), and the uniform structural
 126 coloration of the palettes (of nanodot arrays) correspondingly changed from blue to yellow
 127 (**Fig. 1e**). The SPP mode can be expressed by following equation:

$$Re \left[\frac{\omega}{c} \sqrt{\frac{\epsilon_m \epsilon_d}{\epsilon_m + \epsilon_d}} \right] = |\mathbf{k}_0 \sin \theta + i\mathbf{G}_x + j\mathbf{G}_y| \quad (1)$$

128 where ω , c , θ , and \mathbf{k}_0 are the angular frequency, velocity, incident angle, and momentum of
 129 light in free space, respectively, and the integer index pairs (i, j) denote specific SPP modes. \mathbf{G}_x
 130 and \mathbf{G}_y ($|\mathbf{G}_x| = |\mathbf{G}_y| = 2\pi/P$) represent the grating vectors along the x and y axes generated
 131 by the nanodot arrays⁵³⁻⁵⁵. In our system, ϵ_m is the relative permittivity of silver (ϵ_{silver}) and ϵ_d
 132 corresponds to the effective permittivity of the nanodot array ($\epsilon_{effective}$). For the first-order SPP
 133 mode with a normal incidence of $\theta = 0^\circ$, i.e., $(i, j) = (\pm 1, 0)$ or $(0, \pm 1)$, the wavelength of SPP
 134 resonance (λ_{SPP}) can be simplified as:

$$\lambda_{SPP} = P \sqrt{\frac{\epsilon_{silver} \epsilon_{effective}}{\epsilon_{silver} + \epsilon_{effective}}} \quad (2)$$

135 with the condition of effective permittivity being $\epsilon_{effective} = n_{effective}^2$ ⁵⁶. This eq (2)
 136 illustrates that the red-shift of the SPP resonance occurs with increasing $n_{effective}$ by a gradual
 137 increment of D , which in turn enhances the filling ratio of PVA on Ag; this analysis theoretically
 138 supports the experimental measurements in **Fig. 1d**.

139 In order to understand SPP resonance, we numerically calculated λ_{SPP} with electric near-
 140 field distributions with respect to varying D using finite-difference time-domain (FDTD)

141 simulations. **Fig. 2a** shows that the simulated resonant peak was red-shifted with D ,
142 qualitatively matching the experiments, and the near-field enhancement is stronger at longer
143 wavelengths (from 500 to 512 to 530 nm) with increased D (from 188 to 209 to 237 nm). The
144 FDTD simulation also visualized the field enhancements at the bottom edges of nanodots,
145 which form the characteristic profiles of the SPP mode (**Fig. 2b**). Specifically, a strong
146 enhancement factor of 41.5 was observed at λ_{SPP} of 500 nm where the diameter is relatively
147 small (D of 188 nm), and the intensity factor decreased by 83% as D increased to 237 nm. At
148 λ_{SPP} of 512 nm, a maximum enhancement factor of 42.1 was recorded for a value of D of 209
149 nm. For the longer resonant wavelength (λ_{SPP} of 530 nm), the hydrogel nanodots with D of 188
150 and 209 nm could not induce the concentrated electric field, whereas D of 237 nm generated
151 strong field enhancement (enhancement factor of 42.3). The discrepancy between λ_{SPP}
152 measured by the experiments and the values calculated by the numerical model can be
153 attributed to the surface roughness of the Ag films (**Fig. S2**) which restricts the propagation
154 distance of SPPs^{57,58}.

155 Beyond static tuning of plasmonic resonance based on engineered meta-atom dimensions,
156 the optical properties of the hydrogel-based metasurface could be dynamically controlled in
157 response to a varying environmental moisture level. As the relative humidity (RH) to which
158 the surface was exposed increased from 0.17% RH to 96.9% RH (i.e., saturation), the hydrogel
159 nanodots swelled by absorbing water and their size D increased from 205 to 277 nm as
160 characterized by environmental atomic force microscopy (e-AFM) (**Figs. 3a-b**). The cross-
161 sectional profiles of the e-AFM images also confirm that the height (H) of nanodots was nearly
162 constant irrespective of RH; the lateral volume expansion dominates the system dynamics (**Figs.**

163 **3a-b, Fig. S3**). This observation suggests that the overall volume of the individual nanodot
164 expanded by 182% as RH approached saturation, which resulted in a dynamic red-shift of λ_{SPP}
165 from 542 to 558 nm (**Fig. 3c, Table S1**). In addition, we measured the refractive index of
166 continuous hydrogel films at different RH (using ellipsometry) to detect the thickness change
167 and verified that the hydrogel volume expansion was indeed induced by absorbing water under
168 the applied experimental conditions (**Fig. S4**). The levels of red-shift of around 10~15 nm were
169 quantitatively similar to each other for different values of D for the nanodots (and
170 corresponding different structural coloration), which indicates that the degree of volume
171 expansion was near-identical for all the samples (**Figs. S5 and S6**).

172 We highlight highly stable and reversible tuning over λ_{SPP} from the metasurface with D of
173 188 nm by applying cyclic RH changes; as RH oscillated between 10.3 and 89.4% RH, λ_{SPP}
174 switched between 498 and 505 nm in a cyclic manner which in turn induced continuous
175 structural color changes (between blue and blue-green) (**Fig. 3d and Fig. S7**). We used this
176 dynamic plasmonic coloration as a platform to encode and decode optical information for an
177 anti-counterfeiting application (**Fig. 3e**). The “QR code” shown in this work consists of
178 hydrogel nanodots with two distinct D ($D_1 = 188$ and $D_2 = 192$ nm). The local regions with
179 smaller nanodots (denoted as D_1) induced a resonant λ_{SPP} of 505 nm, whereas the regions with
180 larger nanostructures (denoted as D_2) induced a λ_{SPP} of 511 nm at the initial RH (i.e., 10.3%
181 RH) such that a plasmonic color contrast formed on the metasurface. The dark-field images of
182 the QR code under applied RH between 10.3% and 71.4% exhibited almost negligible color
183 contrast (encoded state) because the difference between D_1 and D_2 is relatively small over this
184 RH range. As RH increased above 89.4%, the contrast was significantly improved (decoded

185 state) because the size difference between D_1 and D_2 was increased significantly; the volume
186 expansion ratio of the nanodots at this level of RH was $\sim 180\%$ (**Figs. 3a-b**). This color
187 coordination and contrast were inconspicuous with bright field imaging, though, because the
188 normal reflection from the light source overlaps with the scattering from the nanodots,
189 cancelling out the optical signal from the metasurface (**Fig. S8**).

190 The reversible structural coloration achieved with the hydrogel metasurface can also
191 benefit applications in multi-color dynamic displays. **Figs. 4a-b** show dark-field images of
192 color printing, where spatially distinct, multi-level color contrast visualizes the “Hangzhou
193 Dianzi University” badge (at 10.3 and 89.4% RH). We printed the badge with three distinct
194 local palettes patterned with different D of hydrogel nanodots at 10.3% RH (**Figs. 4c-f**): (1)
195 regions with yellow and dark red for the frame of the badge (D of 240~250 nm, corresponding
196 λ_{SPP} of 590~600 nm); (2) regions with cyan for the background of the badge core (D of ~ 204
197 nm, corresponding λ_{SPP} of 539 nm); and (3) regions with dark blue for the characters and
198 university symbol of the badge (D of ~ 175 nm, corresponding λ_{SPP} of 495 nm). This multi-
199 color printing approach using a single material and leveraging nanodot-level resolution varies
200 the constituent local coloration by increasing RH up to 89.4% to swell the nanodots (**Fig. 4b**),
201 including instances of: (1) regions with dark red for the frame of the badge (corresponding λ_{SPP}
202 of 605~615 nm); (2) regions with green for the background of the badge core (corresponding
203 λ_{SPP} of 559 nm); and (3) regions with blue for the characters and university symbol of the badge
204 (corresponding λ_{SPP} of 505 nm). Different D of the nanodots can be hierarchically patterned
205 into local palettes with arbitrary geometries, which enables a general platform for
206 environmentally responsive, multi-color high-resolution displays.

207 We further demonstrate that the hydrogel-based metasurfaces can function as a phase
 208 modulator to enable dynamic beam steering over the visible spectrum (**Fig. 5**). Because the
 209 contrast in refractive index over a single hydrogel nanodot is too small to generate sufficient
 210 phase delay at the sub-wavelength scale, we deposited an Ag cap (20 nm-thickness) on top of
 211 the hydrogel nanodots to improve plasmonic phase shift and thereby constructed metal-
 212 insulator-metal gap plasmon resonators (MIM-GPRs, **Fig. S9**). We designed and fabricated the
 213 phase modulator with “super units,” where each super unit consists of nanodots with three
 214 distinct D for MIM-GPRs (**Fig. 5a**). By integrating three MIM-GPRs with different D into the
 215 supercell unit ($3 \times P$), beam steering performance mimicking a blazed grating can be realized
 216 according to the generalized Snell’s Law ⁵⁹:

$$\theta_r = \sin^{-1}\left(\frac{\lambda}{2\pi} \times \frac{\Delta\Phi}{3P} + \sin \theta_i\right) \quad (3)$$

217 where θ_i and θ_r represent the incident and reflective angles of light, respectively, and $\Delta\Phi$
 218 indicates phase increment between adjacent MIM-GPRs. We set the value of P of the
 219 nanostructures to 400 nm to control the incidence over the visible spectrum^{60,61}. We
 220 investigated the relationship between D and the degree of phase shift at different RH and found
 221 that $\Delta\Phi$ reduced with larger RH (**Fig. S10**).

222 As the hydrogel in MIM-GPRs swelled close to its maximum volume under 96.9% RH,
 223 the phase gradient generated by the supercell unit (i.e., $\Delta\Phi/3P$ in eq. (3)) declined drastically
 224 (**Figs. 5b-c**). This phase alternation significantly reduced the phase trending as well as the
 225 deflection power of beam steering to the first diffraction order. To characterize broadband
 226 beam-steering performance, we measured far-field angular distributions under two distinct RH

227 (40% RH and 96.9% RH) and confirmed the ability of our system to achieve environmentally
228 tunable reflection steering to the first diffraction order. In contrast to the beam steering by the
229 phase modulator under 96.9% RH, the outgoing intensity distributions show that the reflected
230 beam is dramatically directed to the first-order direction ($\theta_r \sim 35^\circ$) over the spectrum between
231 680 and 740 nm wavelength under 40% RH (Figs. 5d-e). The measured angular reflection
232 power distributions at 700 nm match well with the calculated spectra both for 40% RH and
233 96.9% RH (Figs. 5d-e). We quantitatively confirmed that the optical intensity at the first
234 diffraction order ($\theta_r \sim 35^\circ$) under 40% RH is 2.1 times greater than the reflection intensity from
235 the surface of the modulator under 96.9% RH; therefore, we can set an OFF state for beam
236 steering (to first diffraction order) with 96.9% RH, while the ON state is triggered when the
237 modulator is exposed to 40.0% RH. Our experimental and theoretical results show that this
238 environmentally responsive phase modulator can steer light beams over the broadband
239 spectrum in a programmable manner.

240 **Discussion**

241 In summary, we developed a general platform for dynamically tunable, hydrogel-based
242 plasmonic metasurfaces. By using high-resolution hydrogel resist for EBL, we constructed
243 hydrogel nanodots hundreds of nanometers in diameter to generate reliable SPPs on silver
244 layers. As the hydrogel nanodots swelled and shrank under varying levels of environmental
245 RH, the peaks of the SPPs were reversibly tuned in response to RH. We demonstrated that
246 these hydrogel metasurfaces can benefit practical applications in anti-counterfeiting and lead
247 to multicolored displays with single-nanodot resolution based on meta-atoms with distinct D
248 being spatially patterned by design. Furthermore, we showed that the arrangement of hydrogel

249 super-cell units enabled a phase modulator to dynamically control the wavefront of visible light
250 reflected from the metasurface. Considering the biocompatibility of hydrogels, we also expect
251 that our responsive materials system will be widely adopted for in-vivo applications in
252 biophotonics

253

254 **Methods**

255 **Fabrication of hydrogel-based plasmonic metasurfaces.** First, silicone (Si) wafers (2 inches,
256 Kaihuajingxin Electronics Co., Ltd.) were cleaned using deionized (DI) water, followed by
257 ultrasonication in acetone and subsequent rinsing with isopropanol. Chromium (Cr) (as an
258 adhesion layer with a thickness of 5 nm) and silver (Ag) (with a thickness of 150 nm) layers
259 were then sequentially deposited on the wafers using thermal evaporation. The hydrogel resist
260 was prepared by dissolving 6 wt.% polyvinyl alcohol (PVA, M_w between 10,000 and 26,000
261 g/mol, degree of alcoholysis 87~89%, Alfa Aesar) in DI water. The resist was spin-coated on
262 the Ag/Cr/Si substrates to form a uniform film-thickness of 150 nm. The hydrogel nanodots
263 were patterned on the resist films using electron beam lithography (EBL, Elphy Quantum
264 system, Raith GmbH) with an acceleration voltage of 2 kV and an electron dose of 0.1~20
265 pC/dot (**Fig. 1c**, **Fig. 3e**, **Fig. 4**, and **Fig. S1**). After exposure, the sample was developed with
266 DI water for 1 min and dried with N_2 gas. The color prints of the QR code and the “Hangzhou
267 Dianzi University” badge in the main text were prepared by grayscale EBL; the original color
268 images were transferred to grayscale bitmaps and each value in the grayscale was designated a
269 corresponding exposure dose in EBL, such that the nanodot arrays with spatially different D
270 for multi-color palettes could be fabricated. The metal-insulator-metal gap plasmon resonators

271 (MIM-GPRs) for the phase modulator were prepared by depositing one Ag layer (thickness of
272 20 nm) on the top of the hydrogel nanodot arrays using thermal evaporation (**Fig. S9**).

273 **Characterization of hydrogel metasurfaces.** The morphologies of hydrogel nanodots were
274 observed using scanning electron microscopy (SEM, Sigma 300, Carl Zeiss) and dark- and
275 bright-field optical microscopy. In particular, the values of D of the nanodots were correlated
276 with the electron dose in EBL based on the corresponding SEM images (**Fig. 1c** and **Fig. S1**).
277 We visualized humidity-responsive, structural coloration of the micro-palettes, including the
278 QR code and the “Hangzhou Dianzi University” badge, using a fiber-coupled optical
279 microscope system for which collection of the scattering spectra and far-field images of the
280 metasurfaces is possible. During the optical characterization, the samples were located in a
281 humidity-controlled box purged with N_2 gas, where the level of relative humidity (RH) was
282 manually controlled between dry (0.2% RH) and saturated (96.9% RH) states. RH was
283 simultaneously recorded with a commercial RH sensor (TSP01, Thorlabs)³⁸. The hydrogel
284 nanodots swell or shrink in response to varying RH, and the resulting three-dimensional (3D)
285 topographies were further characterized by an environmental atomic force microscope (e-AFM,
286 CypherES, Oxford) equipped with a humidity control system that uses gas perfusion through a
287 sealed cell (**Figs. 3a-b, Fig. S3**).

288 **Numerical simulations.** Full-field electromagnetic wave calculations of arrays of hydrogel
289 nanodots and MIM-GPRs were performed using Lumerical, a commercially available FDTD
290 simulation software package (**Fig. 2** and **Fig. 5**). For the simulations in **Fig. 2**, we set a unit cell
291 area of $400 \times 400 \text{ nm}^2$ in x - y plane with periodic boundary conditions and the perfectly
292 matched layers (PMLs) along the propagation of waves in z -axis. Also, the total-field scattered-

293 field (TFSF) source was applied to illuminate the nanodots. For the simulations in **Fig. 5**, we
294 set a plane wave approaching the nanostructures along z direction, and the amplitude and phase
295 of the reflected light were collected with a power monitor placed behind the radiation source.
296 The angular intensity distribution is obtained by far-field analysis from the monitor.

297 **Characterization of beam steering from hydrogel-based phase modulator.** The beam
298 steering performance of the phase modulator patterned with arrays of MIM-GPRs (**Figs. 5d-e**)
299 was captured using a Fourier-transform-based angular-resolved microscope system (ARMS,
300 Ideaoptics) coupled with a spectrometer (Princeton Instruments, SpectraPro HRS-300). The
301 reflected beam intensity as a function of θ_r over the target wavelength spectrum was directly
302 collected by the angle-resolved microscope system without additional data processing⁶².

303
304
305
306
307
308
309
310
311
312
313
314

315 **References**

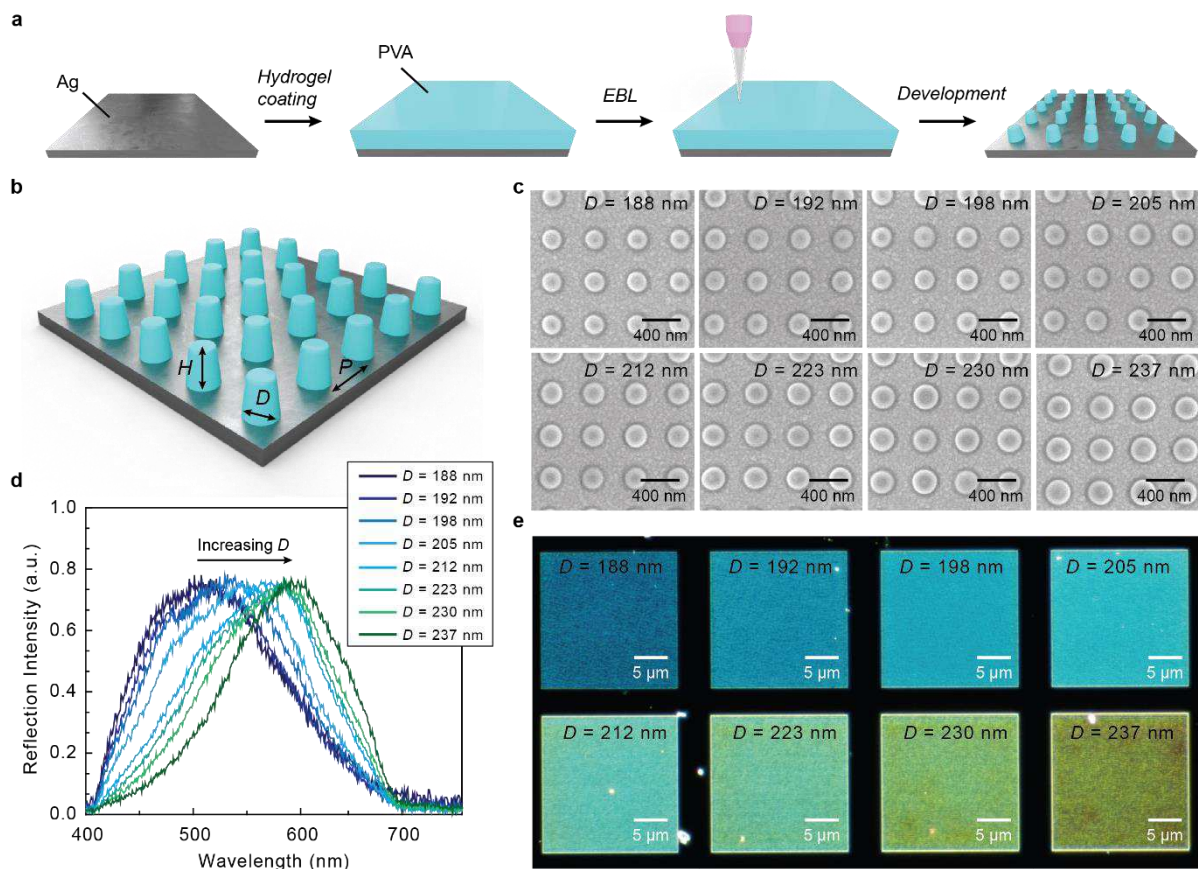
- 316 1 Capasso, F. The future and promise of flat optics: a personal perspective.
317 *Nanophotonics* **7**, 953-957 (2018).
- 318 2 Chen, W. T., Zhu, A. Y. & Capasso, F. Flat optics with dispersion-engineered
319 metasurfaces. *Nat. Rev. Mater.* **5**, 604-620 (2020).
- 320 3 Meinzer, N., Barnes, W. L. & Hooper, I. R. Plasmonic meta-atoms and metasurfaces.
321 *Nat. Photonics* **8**, 889-898 (2014).
- 322 4 Kildishev, A. V., Boltasseva, A. & Shalaev, V. M. Planar photonics with metasurfaces.
323 *Science* **339**, 1232009 (2013).
- 324 5 Hu, J. *et al.* Lattice-resonance metalenses for fully reconfigurable imaging. *ACS Nano*
325 **13**, 4613-4620 (2019).
- 326 6 Bin-Alam, M. S. *et al.* Ultra-high-Q resonances in plasmonic metasurfaces. *Nat.*
327 *Commun.* **12**, 1-8 (2021).
- 328 7 Metzger, B. *et al.* Strong enhancement of second harmonic emission by plasmonic
329 resonances at the second harmonic wavelength. *Nano Lett.* **15**, 3917-3922 (2015).
- 330 8 You, J. W., Lan, Z. & Panoiu, N. C. Four-wave mixing of topological edge plasmons in
331 graphene metasurfaces. *Sci. Adv.* **6**, eaaz3910 (2020).
- 332 9 Roberts, A. S., Pors, A., Albrektsen, O. & Bozhevolnyi, S. I. Subwavelength plasmonic
333 color printing protected for ambient use. *Nano Lett.* **14**, 783-787 (2014).
- 334 10 Jin, Y. *et al.* Electrical dynamic switching of magnetic plasmon resonance based on
335 selective lithium deposition. *Adv. Mater.* **32**, 2000058 (2020).
- 336 11 Ee, H.-S. & Agarwal, R. Tunable metasurface and flat optical zoom lens on a stretchable
337 substrate. *Nano Lett.* **16**, 2818-2823 (2016).
- 338 12 Zhang, X. G. *et al.* An optically driven digital metasurface for programming
339 electromagnetic functions. *Nat. Electron.* **3**, 165-171 (2020).
- 340 13 Duan, X., Kamin, S. & Liu, N. Dynamic plasmonic colour display. *Nat. Commun.* **8**, 1-
341 9 (2017).
- 342 14 Wang, D. *et al.* Stretchable nanolasing from hybrid quadrupole plasmons. *Nano Lett.*
343 **18**, 4549-4555 (2018).
- 344 15 Malek, S. C., Ee, H.-S. & Agarwal, R. Strain multiplexed metasurface holograms on a
345 stretchable substrate. *Nano Lett.* **17**, 3641-3645 (2017).
- 346 16 Lininger, A. *et al.* Optical properties of metasurfaces infiltrated with liquid crystals.
347 *Proc. Natl. Acad. Sci. U. S. A.* **117**, 20390-20396 (2020).
- 348 17 Neubrech, F., Duan, X. & Liu, N. Dynamic plasmonic color generation enabled by

- 349 functional materials. *Sci. Adv.* **6**, eabc2709 (2020).
- 350 18 Yang, A. *et al.* Real-time tunable lasing from plasmonic nanocavity arrays. *Nat.*
351 *Commun.* **6**, 1-7 (2015).
- 352 19 Hu, Y. *et al.* Electrically tunable multifunctional polarization-dependent metasurfaces
353 integrated with liquid crystals in the visible region. *Nano Lett.* **21**, 4554-4562 (2021).
- 354 20 Franklin, D., Frank, R., Wu, S.-T. & Chanda, D. Actively addressed single pixel full-
355 colour plasmonic display. *Nat. Commun.* **8**, 1-10 (2017).
- 356 21 Liu, Q., Yuan, Y. & Smalyukh, I. I. Electrically and optically tunable plasmonic guest-
357 host liquid crystals with long-range ordered nanoparticles. *Nano Lett.* **14**, 4071-4077
358 (2014).
- 359 22 Yan, Z. *et al.* Floating solid-state thin films with dynamic structural colour. *Nat.*
360 *Nanotechnol.* **16**, 795-801 (2021).
- 361 23 Huang, Y.-W. *et al.* Gate-tunable conducting oxide metasurfaces. *Nano Lett.* **16**, 5319-
362 5325 (2016).
- 363 24 Abdollahramezani, S. *et al.* Dynamic hybrid metasurfaces. *Nano Lett.* **21**, 1238-1245
364 (2021).
- 365 25 Gholipour, B. *et al.* Phase-change-driven dielectric-plasmonic transitions in
366 chalcogenide metasurfaces. *NPG Asia Mater.* **10**, 533-539 (2018).
- 367 26 Kim, Y. *et al.* Phase modulation with electrically tunable vanadium dioxide phase-
368 change metasurfaces. *Nano Lett.* **19**, 3961-3968 (2019).
- 369 27 Shu, F. Z. *et al.* Dynamic plasmonic color generation based on phase transition of
370 vanadium dioxide. *Adv. Opt. Mater.* **6**, 1700939 (2018).
- 371 28 Li, J. *et al.* Direct evidence of reactive ion etching induced damages in Ge₂Sb₂Te₅
372 based on different halogen plasmas. *Appl. Surf. Sci.* **378**, 163-166 (2016).
- 373 29 Kang, S.-K., Jeon, M.-H., Park, J.-Y., Jhon, M. S. & Yeom, G.-Y. Etch damage of
374 Ge₂Sb₂Te₅ for different halogen gases. *Jpn. J. Appl. Phys.* **50**, 086501 (2011).
- 375 30 Yoon, S.-M. *et al.* Dry etching of Ge₂Sb₂Te₅ thin films into nanosized patterns using
376 TiN hard mask. *Jpn. J. Appl. Phys.* **45**, L1080 (2006).
- 377 31 Kim, C. *et al.* Direct evidence of phase separation in Ge₂Sb₂Te₅ in phase change
378 memory devices. *Appl. Phys. Lett.* **94**, 193504 (2009).
- 379 32 Duan, X. & Liu, N. Magnesium for dynamic nanoplasmonics. *Acc. Chem. Res.* **52**,
380 1979-1989 (2019).
- 381 33 Chen, Y. *et al.* Dynamic color displays using stepwise cavity resonators. *Nano Lett.* **17**,
382 5555-5560 (2017).

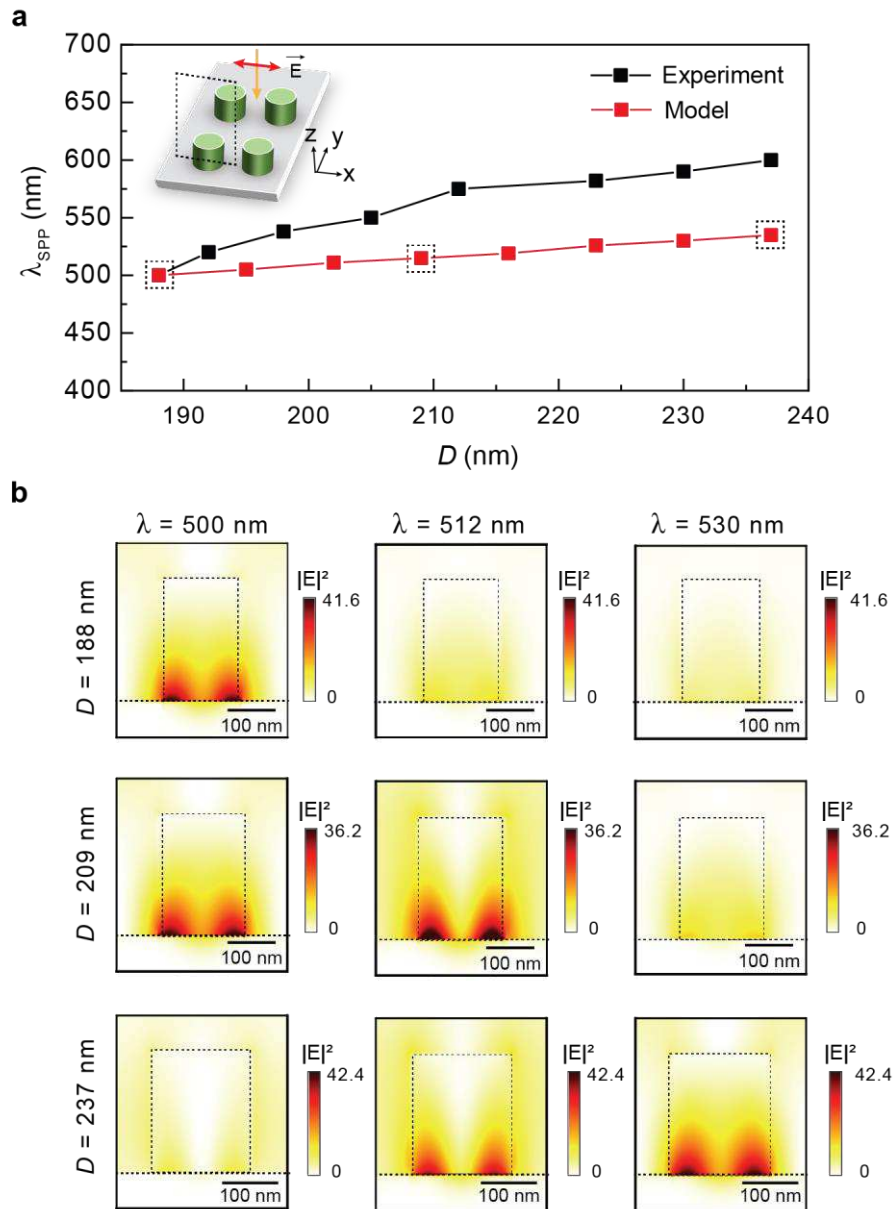
- 383 34 Cui, X. F. *et al.* Water-retaining, tough and self-healing hydrogels and their uses as fire-
384 resistant materials. *Polym. Chem.* **10**, 5151-5158 (2019).
- 385 35 Chivers, P. R. & Smith, D. K. Shaping and structuring supramolecular gels. *Nat. Rev.*
386 *Mater.* **4**, 463-478 (2019).
- 387 36 Yu, Y. *et al.* Nanostructured lipid carrier-based pH and temperature dual-responsive
388 hydrogel composed of carboxymethyl chitosan and poloxamer for drug delivery. *Int. J.*
389 *Biol. Macromol.* **114**, 462-469 (2018).
- 390 37 Asoh, T. a., Matsusaki, M., Kaneko, T. & Akashi, M. Fabrication of Temperature-
391 Responsive Bending Hydrogels with a Nanostructured Gradient. *Adv. Mater.* **20**, 2080-
392 2083 (2008).
- 393 38 Qin, J., Chen, Y.-H., Ding, B., Blaikie, R. J. & Qiu, M. Efficient plasmonic gas sensing
394 based on cavity-coupled metallic nanoparticles. *J. Phys. Chem. C* **121**, 24740-24744
395 (2017).
- 396 39 Lee, Y., Song, W. & Sun, J.-Y. Hydrogel soft robotics. *Mater. Today Phys.* **15**, 100258
397 (2020).
- 398 40 Zhao, Y. *et al.* Soft phototactic swimmer based on self-sustained hydrogel oscillator.
399 *Sci. Rob.* **4**, eaax7112 (2019).
- 400 41 Gao, R. *et al.* A highly homogeneous polymer composed of tetrahedron-like monomers
401 for high-isotropy expansion microscopy. *Nat. Nanotechnol.* **16**, 698-707 (2021).
- 402 42 Fu, F. *et al.* Bio-inspired self-healing structural color hydrogel. *Proc. Natl. Acad. Sci.*
403 *U. S. A.* **114**, 5900-5905 (2017).
- 404 43 Fu, F., Shang, L., Chen, Z., Yu, Y. & Zhao, Y. Bioinspired living structural color
405 hydrogels. *Sci. Rob.* **3**, eaar8580 (2018).
- 406 44 Tian, E. *et al.* Colorful humidity sensitive photonic crystal hydrogel. *J. Mater. Chem.*
407 **18**, 1116-1122 (2008).
- 408 45 Chen, D. *et al.* Dynamic tunable color display based on metal–insulator–metal
409 resonator with polymer brush insulator layer as signal transducer. *ACS Appl. Mater.*
410 *Interfaces* **11**, 41668-41675 (2019).
- 411 46 Ge, Q. *et al.* 3D printing of highly stretchable hydrogel with diverse UV curable
412 polymers. *Sci. Adv.* **7**, eaba4261 (2021).
- 413 47 Zhang, W. *et al.* Structural multi-colour invisible inks with submicron 4D printing of
414 shape memory polymers. *Nat. Commun.* **12**, 1-8 (2021).
- 415 48 Quilis, N. G. *et al.* UV-Laser Interference Lithography for Local Functionalization of
416 Plasmonic Nanostructures with Responsive Hydrogel. *J. Phys. Chem. C* **124**, 3297-
417 3305 (2020).

- 418 49 Dang, T.-D., Kim, Y. H., Choi, J. H. & Kim, G.-M. A novel simple preparation method
419 of a hydrogel mold for PDMS micro-fluidic device fabrication. *J. Micromech.*
420 *Microeng.* **22**, 015017 (2011).
- 421 50 Zhang, J. *et al.* Polyvinyl alcohol: a high-resolution hydrogel resist for humidity-
422 sensitive micro-/nanostructure. *Nanotechnology* **31**, 425303 (2020).
- 423 51 Dai, Q., Lee, S.-Y., Lee, S.-H., Kim, B.-G. & Cho, H.-K. Experiment-based estimation
424 of point spread function in electron-beam lithography: Forward-scattering part.
425 *Microelectron. Eng.* **88**, 3054-3061 (2011).
- 426 52 Baburin, A. S. *et al.* Silver-based plasmonics: golden material platform and application
427 challenges. *Opt. Mater. Express* **9**, 611-642 (2019).
- 428 53 Callewaert, F., Chen, S., Butun, S. & Aydin, K. Narrow band absorber based on a
429 dielectric nanodisk array on silver film. *J. Opt.* **18**, 075006 (2016).
- 430 54 Ao, X., Wang, D. & Odom, T. W. Enhanced fields in mirror-backed low-index dielectric
431 structures. *ACS Photonics* **6**, 2612-2617 (2019).
- 432 55 Crescitelli, A. *et al.* Nanostructured metallo-dielectric quasi-crystals: towards photonic-
433 plasmonic resonance engineering. *Adv. Funct. Mater.* **22**, 4389-4398 (2012).
- 434 56 Yang, A. *et al.* Unidirectional lasing from template-stripped two-dimensional
435 plasmonic crystals. *ACS Nano* **9**, 11582-11588 (2015).
- 436 57 Kolomenski, A., Kolomenskii, A., Noel, J., Peng, S. & Schuessler, H. Propagation
437 length of surface plasmons in a metal film with roughness. *Appl. Opt.* **48**, 5683-5691
438 (2009).
- 439 58 Huang, J.-S. *et al.* Atomically flat single-crystalline gold nanostructures for plasmonic
440 nanocircuitry. *Nat. Commun.* **1**, 1-8 (2010).
- 441 59 Yu, N. *et al.* Light propagation with phase discontinuities: generalized laws of reflection
442 and refraction. *Science* **334**, 333-337 (2011).
- 443 60 Hu, Y. *et al.* 3D-Integrated metasurfaces for full-colour holography. *Light Sci. Appl.* **8**,
444 1-9 (2019).
- 445 61 Lee, G.-Y. *et al.* Metasurface eyepiece for augmented reality. *Nat. Commun.* **9**, 1-10
446 (2018).
- 447 62 Li, Z. *et al.* Actively Switchable Beam-Steering via Hydrophilic/Hydrophobic-
448 Selective Design of Water-Immersed Metasurface. *Adv. Opt. Mater.* **9**, 2100297 (2021).

449
450
451
452



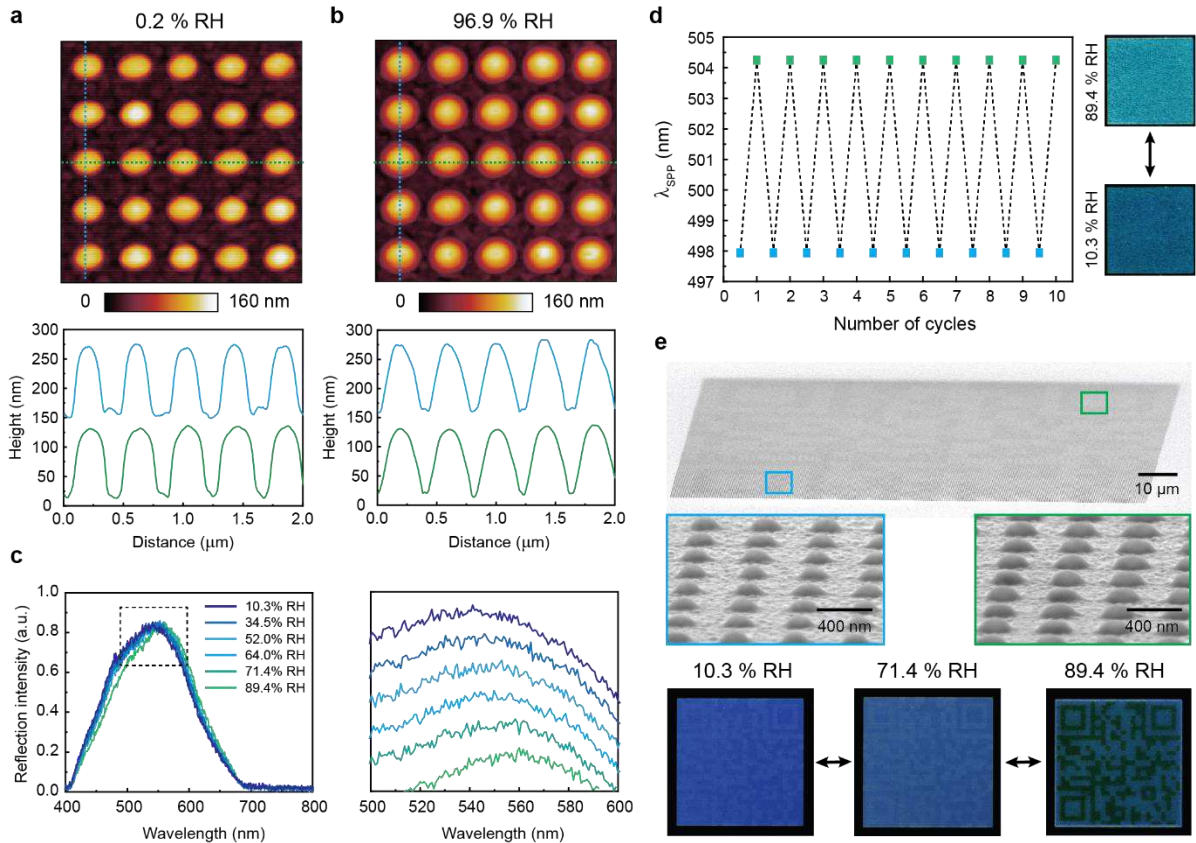
457 **Fig. 1.** (a) Fabrication of hydrogel nanodot arrays on silver films using EBL. (b) Schematic of
 458 the hydrogel-based metasurface with characteristic features (D , H , and P). (c) Scanning
 459 electron microscopy (SEM) images of hydrogel nanodot arrays with different D (D from 188
 460 nm to 237 nm). (d) Reflectance spectra of the metasurfaces with varying D and (e) dark-field
 461 microscope images of the micro-palettes with hydrogel nanodot arrays with values of D
 462 corresponding to (c).



463

464

465 **Fig. 2. (a)** Measured and simulated λ_{SPP} as a function of D . **(b)** Near-field distributions of
 466 electromagnetic fields ($|E|^2$) along nanodots with D of 188, 209, and 237 nm at the wavelengths
 467 of 500, 512, and 530 nm. The field distributions were visualized in the x - z planes of a single
 468 nanodot as presented in the inset of (c).



469

470

471

472

473

474

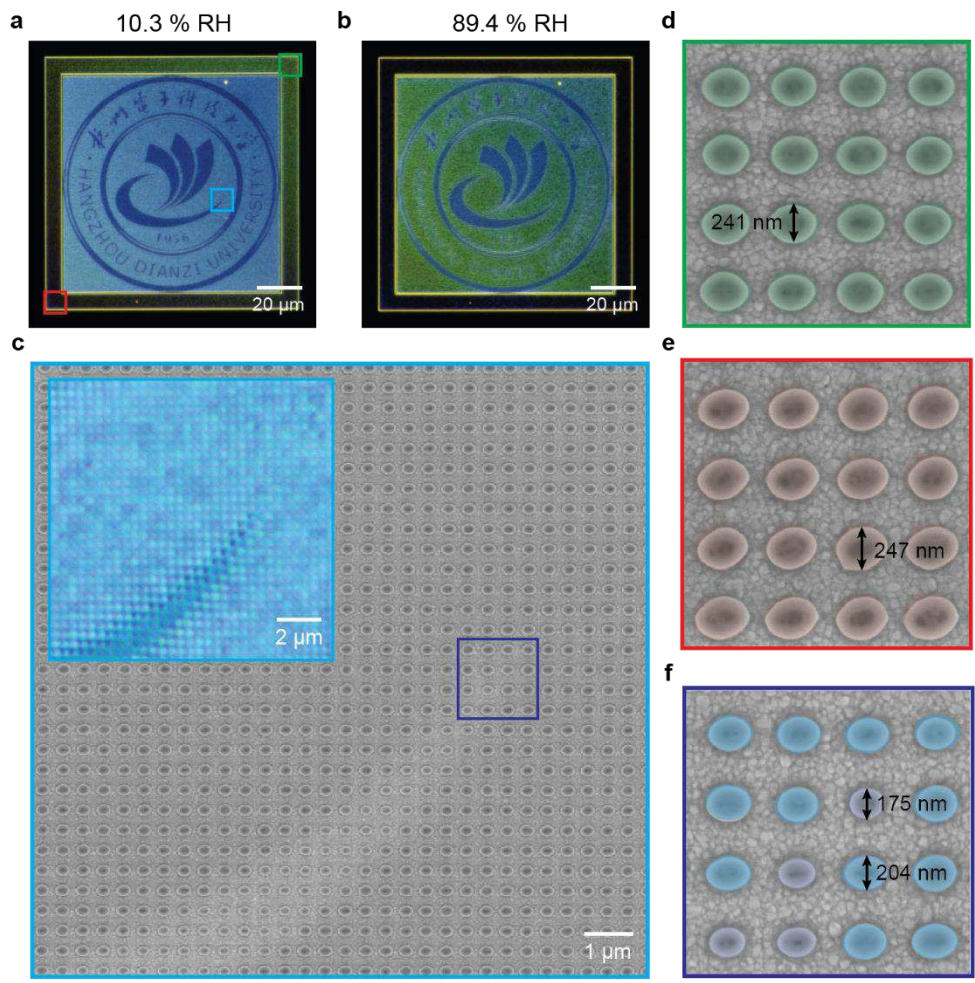
475

476

477

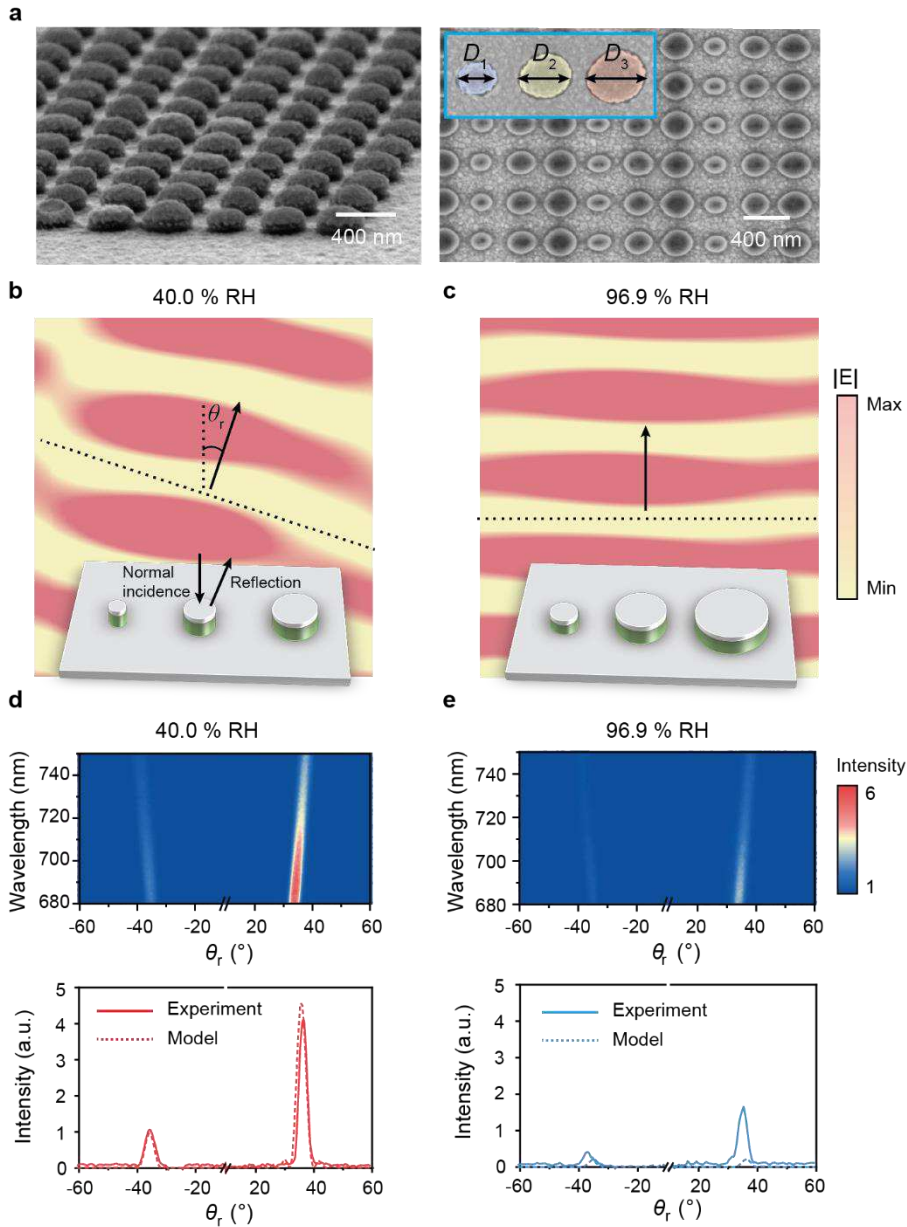
478

Fig. 3. e-AFM images of hydrogel nanodots with P of 400 nm at (a) dry (0.2% RH) and (b) saturated RH ($\sim 97\%$ RH), and corresponding cross section profiles. (c) Reflectance spectra of the metasurfaces with the nanodots with varying RH. The red-shift of λ_{SPP} with increasing RH is shown from the enlarged spectra. (d) Oscillation of λ_{SPP} and structural coloration from the hydrogel metasurface with cyclic variation of RH between 10.3 and 89.4%. The size of the palette is $20 \times 20 \mu\text{m}^2$. (e) SEM images of the QR code consisting of different D ($D_1 = 188$ nm in cyan box and $D_2 = 192$ nm in green box) of nanodots and dark-field optical microscopy images of the code under 10.3, 71.4, and 89.4% RH. The size of the QR code is $100 \times 100 \mu\text{m}^2$.



479
480

481 **Fig. 4.** Dark-field optical microscopy images of the color printing with “Hangzhou Dianzi
482 University” badge at **(a)** 10.3% and **(b)** 89.4% RH. **(c)** SEM image of the local area (marked
483 with cyan box) in (a) where nanodots with two distinct D were spatially patterned. The inset
484 shows the optical microscopy image over the same area. Zoomed-in SEM images of local areas
485 marked with **(d)** green and **(e)** red box in (a), and **(f)** blue box in (c).



486

487

488

489

490

491

492

493

Fig. 5. (a) SEM images with tilted (left) and top-view (right) of the phase modulator patterned with supercell units consisting of three hydrogel nanodots with gradually increasing D . Inset image resolves varying D of a single unit ($D_1 = 120$ nm, $D_2 = 160$ nm, $D_3 = 200$ nm). Wavefront evolution from the phase modulator under (b) 40.0 and (c) 96.9% RH. Measured two-dimensional far-field angular distribution contours of the reflected beam at P-wave normal incidence, and experimental and simulated angular reflection intensity distributions at the wavelength of 700 nm under (d) 40.0 and (e) 96.9% RH.

494 **Acknowledgments**

495 The authors gratefully acknowledge National Key Research and Development Program of
496 China (2019YFE0121700), National Key Scientific Instrument and Equipment Development
497 Project of China (51927802), Zhejiang Provincial Key Research and Development Program
498 (2019C01121), Start-up Program of Hangzhou Dianzi University (KYS385618067), and the
499 Fundamental Research Funds for the Provincial Universities of Zhejiang (GK219909299001-
500 003). The authors thank the supports from the Key Laboratory of 3D Micro/Nano Fabrication
501 and Characterization of Zhejiang Province and Instrumentation and Service Center for Physical
502 Sciences in Westlake University. W-K. Lee acknowledges support from the National Research
503 Foundation of Korea (NRF) grant funded by the Korean government (MSIT) (No.
504 2021R1F1A1047037).

505

506 **Author contributions**

507 J.Z, Q.L, C.D, Z.L, X.Z, W.K.L conceived the work; J.Z, Q.L, C.D, M.C, X.H fabricated the
508 metasurfaces; J.Z, Q.L, C.D, M.C, X.H, Z.L, X.Z, W.K.L contributed to experimental setup
509 and collection and interpretation of data; J.Z, C.D, Z.L developed the numerical model; J.Z,
510 H.S.K, H.Y, D.J.P, Z.L, X.Z, W.K.L wrote and revised the manuscript; Z.L, X.Z, W.K.L
511 oversaw the work.

512

513 **Competing interests**

514 All other authors declare they have no competing interests.

515

516 **Data and materials availability**

517 All data needed to evaluate the conclusions in the article are present in the main text or the
518 Supplementary Materials.

519

520

521

522

523

524

525

526

527 **Supplementary Materials**

528

529 Fig. S1. Relationship between D of hydrogel nanodots and electron dose in EBL.

530 Fig. S2. Surface roughness of Ag film.

531 Fig. S3. 3D topographies of hydrogel nanodots before and after swelling.

532 Fig. S4. Experimental and theoretical analysis of hydrogel swelling mechanism.

533 Fig. S5. Relationships between the range of λ_{SPP} and D with varying RH.

534 Fig. S6. Structural coloration of the micro-palettes with different.

535 Fig. S7. Reversible control of λ_{SPP} by cyclic RH variation.

536 Fig. S8. Bright-field optical microscope image of “QR code” pattern.

537 Fig. S9. Fabrication processes of MIM-GPRs.

538 Fig. S10. Phase shift from supercell units with different D .

539

540 Table S1. Quantified humidity-driven redshifts of λ_{SPP} for different D .

Supplementary Files

This is a list of supplementary files associated with this preprint. Click to download.

- [SI.pdf](#)